RESEARCH: Original Research

Advanced interfacial phase change material: Structurally confined and interfacially extended superlattice

Hyeonwook Lim [a], Youngsam Kim [b], Kyu-Jin Jo [c], Choi Seok [d], Chang Woo Lee [a], Dasol Kim [a], Gihyeon Kwon [a], Hoedon Kwon [a], Soobin Hwang [a], Kwangsik Jeong [e], Byung-Joon Choi [d], Cheol-Woong Yang [c], Eunji Sim [b], Mann-Ho Cho [a,*]

[a] Department of Physics, Yonsei University, 50 Yonsei-ro, Seoul 03722, Republic of Korea
[b] Department of Chemistry, Yonsei University, 50 Yonsei-ro, Seoul, Republic of Korea
[c] School of Advanced Materials of Science and Engineering, Sungkyunkwan University, 2066 Seobu-ro, Suwon, Gyeonggi-do 16419, Republic of Korea
[d] Department of Materials Science and Engineering, Seoul National University of Science and Technology, 232 Seoul, Republic of Korea
[e] Division of Physics and Semiconductor Science, Dongguk University, Seoul, Republic of Korea

Interfacial Phase Change Memory (iPCM) retrench unnecessary power consumption due to wasted heat generated during phase change by reducing unnecessary entropic loss. In this study, an advanced iPCM (GeTe/Ti-Sb_2Te_3 Superlattice) is synthesized by doping Ti into Sb_2Te_3. Structural analysis and density functional theory (DFT) calculations confirm that bonding distortion and structurally well-confined layers contribute to improve phase change properties in iPCM. Ti-Sb_2Te_3 acts as an effective thermal barrier to localize the generated heat inside active region, which leads to reduction of switching energy. Since Ge-Te bonds adjacent to short and strong Ti-Te bonds are more elongated than the bonds near Sb-Te, it is easier for Ge atoms to break the bond with Te due to strengthened Peierls distortions (R_{long}/R_{short}) during phase change process. Properties of advanced iPCM (cycling endurance, write speed/energy) exceed previous records. Moreover, well-confined multi-level states are obtained with advanced iPCM, showing potential as a neuromorphic memory. Our work paves the way for designing superlattice based PCM by controlling confinement layers.

Keywords: Interfacial phase change materials; Doping; vdW layer; Superlattice; Neuromorphic

Introduction

Phase change memory (PCM) is one of the promising candidates for next-generation non-volatile memory (NVM) while it presents the characteristic of clear electrical/optical contrast with applied variables such as Joule heating or laser irradiation process. In general, PCM has two reversible phases: i.e., a crystal phase (SET states; Low Resistance States [LRS]) based on the 1st stable local structure and an amorphous phase (RESET states; High Resistance States [HRS]) caused by the 2nd stable local structure mixed with 1st stable one. There have been many attempts to design superior PCMs based on single phase materials mainly composed of Ge, Sb, Te alloys [1]. However, there remains a fatal problem: the unnecessary diffusion of heat through the liquid phase generated during the RESET process due to the melt-quenching process [2]. To solve these problems, many research has been conducted on various methods such as pulse design optimization, device structure improvement, and material design to present new paradigms for designing advanced PCMs [3–5]. Meanwhile, outstanding device characteristics for interfacial phase change memory (iPCM) composed of alternately stacked GeTe (GT) and Sb_2Te_3 (ST) within nm ranges

* Corresponding author.
E-mail address: Cho, M.-H. (mh.cho@yonsei.ac.kr)

 https://doi.org/10.1016/j.mattod.2023.07.025

has been reported [6–8]. The main characteristic of iPCM is that two reversible phases are correspond to crystal and metastable crystal phases, not the crystalline and amorphous phases [9,10]. Furthermore, it was reported that iPCM saves energy because it does not undergo a melting process which consumes a lot of the energy generated from heat diffusion in the liquid state during the RESET process [7]. However, due to difficult manufacturing process and complex structure, controversy over the phase change mechanism of iPCM continues and several research which are conflicting with the initially proposed non-melting process have been recently reported [11–13]. In above research, it was well explained that the inner structure of the superlattice exist as GST-like blocks by strong intermixing even if GT and ST are alternately synthesized individually, and the phase change operation also proceeds through a melt-quenching process like the conventional GST alloy. In case of the reduced Reset current for the GST superlattice, it was suggested that an efficient joule heating process was possible by significantly lowered cross-plane thermal conductivity and increased thermal resistance due to the existence of the vdW layers, which can contribute to the phonon scattering in the vicinity of the interfacial region. In addition, recent research based on studies based on in-situ TEM measurements according to the thermal treatment also presented the phase change mechanism of GT/ST SL that it is a thermodynamically driven process and identified through observing vacancy ordering process [14,15]. It was also recently reported that phase change process is progressed through an ultrafast interfacial crystallization process from a transient molten phase for the GT/ST SL [9]. It is innovative suggestion in that phase change process of GT/ST SL is not simply regarded as a melt-quenching process like conventional phase change materials, but both reversible phases of superlattice structure maintain different crystal structures of trigonal/cubic GST even though the transition process contains partial melting process. In addition, it was also reported that the crystallization speed is improved several times by changing the crystallization method of GST SL from the nucleation dominant method to the growth dominant method by characteristics of the "stickier"-surface ST layer, which serves as thermal templates in the SL structure [16]. Although the phase change mechanism of iPCM has not been fully comprehended, many reports suggest that difference between the two phases is determined by local movement of atoms adjacent to interface near the vdW layer [17,18]. Some models for iPCM were suggested based on four representative structures: Petrov, inverted Petrov, Kooi, and Ferro [19]. Structures corresponding to low/high resistance states (LRS/HRS) are considered as Ferro and inverted Petrov, according to Junji Tominaga et al. [20]. While the phase change processes based on the representative models of the GT/ST SL are concentrated only for the vertical motion, it was also reported that the phase change process can be accurately described by including the lateral motion of the GeTe sublayer as 2 step process [21]. Among the various phase change mechanisms proposed for GT/ST SL, there were many models based on changes of Ge atoms' bonding motif. As ST layer being capable of applying strain to the adjacent GT layer, interesting research were reported that the switching energy can be lowered by engineering bi-axial strain applied to GeTe by changing the thickness of the existing Sb_2Te_3 layer or Sb_2Te_1 layer, which is replaced with Sb_2Te_3 layer [22,23]. In these studies, the transition process was also supported through density functional molecular dynamics. Despite the deficient evidence on the properties of each phase in iPCM for the switching process, advanced results which include ultralow-switching current and multi-level characteristics with the GT/ST superlattice on flexible substrates were reported [24]. However, this remarkable performance is limited to specific device structures such as pore-type structures and thermally insulating flexible substrates. Sufficient attempts have not been made to develop advanced iPCM using modified structures by doping with transition metals, such as Sc and Ti, which are already used in alloy-based PCM [25–26]. Recently, phase change heterostructure (PCH), which is composed of the superlattice structure with $TiTe_2$ and ST, showed significantly improved phase change characteristics with the new paradigm to manage thermal transport in the superlattice structure by manipulating the interfacial thermal resistance [27]. Using the thermally stable structure of $TiTe_2$, since the partial crystalline structure can be effectively controlled, multi-level states were successfully obtained. However, despite the results on the superior properties of these superlattice-based phase change materials, and besides the report on the two representative iPCM cases above, only few follow-up studies to devise advanced superlattice structures have been reported. To progress the superlattice based PCM device, further research is needed to maximize advantages of superlattice structure and reduce difficulties in the fabrication process.

In this study, advanced iPCM composed of alternately stacked GT and Ti-doped Sb_2Te_3 (Ti-ST) were synthesized with MBE and evaluated by various measurements. Furthermore, outstanding figure of merits were obtained with the advanced iPCM, including ultra-low power consumption (~2 pJ), high cycling endurance (~3×10^9), fast speed (~8 ns) and multi-level characteristics (~7 level). Considering structural analysis and various experimental measurements, appropriate unit cells are constructed, and density functional theory (DFT) calculations are used to investigate atomic switching characteristics within the microstructure. The structural confinement and interfacial extension of iPCM with Ti atoms enable the above advancement. Phase change process is facilitated by strengthened thermal confinement of Ti-ST blocks and the improved structural coherence near the interface. Peierls distortions of the Ge-Te bonds vicinity to Ti atoms are strengthened due to robust Ti-Te bonding and expansion of the interfacial distance by intra-structural localization of Ti-ST blocks, which also enables triggered Ge atoms to change bonding motifs through smooth atomic movement. Due to the well-controlled interfacial thermal confinement and intra-structural localization of Ti-ST layers, multi-levels with electrical pulsing are obtained. Above properties will pave the way for designing iPCM as a neuromorphic memory, in addition to their application in PCM [28,29].

Furthermore, in the case of alloy-based PCM such as GST, phase change proceeds from random positions during the phase change process. Therefore, as a method of improving phase change characteristics of these thin films, material design is used to directly modify the entire region with several dopants [25–30]. In this study, material design of superlattice system is optimized by selectively modifying confinement layer (from ST to Ti-ST) to

improve phase change properties in intermixed GT layer, which is the activated region surrounded by the confinement layers. Therefore, a new methodology for improving phase change characteristics of PCM is established by engineering the certain confinement layers, not homogeneously. Strong features of iPCM are further improved by reducing unnecessary entropic loss during phase change process, while confinement layers of the system maintain their crystallinity and facilitate the phase change of the intermixed GT layers as efficient intrinsic thermal barriers. It is a new paradigm that it leads to an advancement of phase change characteristics of the entire system by improving the properties of the confinement layer surrounding changeable materials, rather than directly modifying activated region which has been conducted in alloy based PCM. Through the results of this study, it is not just to develop a superlattice material with excellent phase change characteristics, but also to establish a new methodology to design new PCM to ensure its versatility as an efficient gateless memory, such as a neuromorphic memristor which is an essential component to conduct deep learning operation in cross bar array architecture, where the matrix–vector multiplication can be conducted [29,31].

Results and discussion

Electrical evaluation for the GT/Ti-ST superlattice device

The structures of GST-based superlattice device and characteristic changes caused by Ti incorporation are expressed as a schematic using atomic modeling (Fig. 1a). The feature of interfacial expansion along the vertical direction due to Ti doped in ST blocks and locally stretched Ge-Te bonds with distortion are presented. Adopting increasing step pulse programing (ISPP) method (Fig. 1b and Supplementary Fig. 2b), phase change characteristics are evaluated through device operation on the same device platform. For GT/Ti-ST SL, all figure of merits obtained by electrical evaluations are improved compared to GT/ST SL and even other PCMs (Fig. 1c-g).

Advanced iPCM's characteristics showed much better performance in cycling endurance test with a significantly higher value ($\sim 3 \times 10^9$) than the other representative phase change materials including iPCM (Supplementary Fig. 2a, c-d). Compared with GT/ST SL, it is confirmed that reversible resistance states obtained with different electrical pulses are much more confined in GT/Ti-ST SL, which is an important property that prevents each state from overlapping when various resistance states are implemented for multi-level systems. These advancements are detailed in Table 1. As Ti concentration increases above certain level (about 10%), Ti-ST blocks decompose to Ti-ST and $TiTe_2$ phases occurs, which degrade the phase change characteristics (Supplementary Fig. 2e-f, Supplementary Fig. 3f-g) [32]. Multi-level states are also obtained by repeatedly applying different electrical pulses. It is advantageous for resistance-based memories to implement a multi-level cell (MLC) that can be used as a neuromorphic memory [33,34]. Although MLC characteristics have been implemented and reported by previous studies in the use of PCM as a resistance-based memory [35], a gradual change in resistance caused by phase change is very difficult. Herein, confined multi-level resistance states in GT/Ti-ST SL are well implemented with applied different repetitive electrical pulses, and the resistance drift of each resistance state over time was also measured after each different single electric pulse was applied to the device cell (Fig. 1g, Supplementary Fig. 8). Although a similar attempt was conducted with Y doped ST, only three different resistance states with unstable operating process were reported [36]. For iPCM, multi-level states are well implemented with suppressed resistance drift (Supplementary Fig. 8) due to the Ti-ST layers which act as thermal/structural confinement barriers, where the role of the barrier effect has been further strengthened with incorporated Ti element in ST layers, resulting in efficient phase change with high structural/thermal stability (Fig. 5a-e, Supplementary Fig. 9).

Enhanced phase change properties owing to bonding characteristics with Ti

It is observed structural modification at the atomic level after device operation through transmission electron microscopy (TEM) measurement (Fig. 2 and Supplementary Fig. 3). Fig. 2a shows the device structure with HR-TEM after applying electrical signals alternatively about 500,000 times. It is confirmed that the parts maintaining the layered structure are strongly aligned along the c-axis direction (Fig. 2c, e-g). Fig. 2d includes amorphous region where repetitive phase change operations are assumed to be difficult and Fig. 2e shows locally amorphized region incorporated in the layered structure, which is still operable. Septuple and nonuple Te-terminated atomic layers are observed using intensity profiling in high-angle annular dark-field scanning TEM (HAADF-STEM), which are presented in Fig. 2f-g. Among the four representative models suggested by several studies on iPCM (inverted Petrov, Petrov, Ferro, and Kooi models), switching characteristics can be explained by Ferro and inverted Petrov models [17]. The internal structures of the superlattice devices after about 500,000 cycling operations include the Te-terminated intermixed blocks with HCP QL Sb_2-Te_3 layers. Te-terminated layers with cation intermixing can correspond to Ferro-like or Kooi-like structures [17,37], so the thick Te-terminated layers inside iPCM correspond either to Kooi or Ferro structure [38]. However, Kooi structure is so stable that phase change is not possible in it [39]. Considering intensity profiled images of the asymmetric cation sites, the layers might be assumed to correspond with Ferro and Ferro-like structure. In addition, the electrical resistance of the device cell (Fig. 2) was measured as several k ohms after about 500,000 cycle operation. When structural change occurs in LRS phase of GT/Ti-ST SL due to laser irradiation, the valence electrons occupied in 4 s orbital of Ge participate in chemical bonding while forming sp3 hybridized tetrahedral bond (covalent bond) with adjacent Te, which breaks the previously well-maintained p orbital alignment (LRS) in the vicinity of the vdW layer (Supplementary Fig. 7) [40]. While the ordering of the anion layers in the SL structure is strongly maintained by applied thermal/electrical input, it is observed that diffusion of cation atoms occurred to some extent. Since it is confirmed that only the chemical states of the Ge atoms change with in-situ X-ray photoelectron spectroscopy (XPS) measurements, the phase change process of GT/(Ti)-ST SL occurs through site switching between Ge atoms adjacent to vdW layers and vacancies (Supplementary Fig. 10). Therefore, the memory state of the measured device cell (Fig. 2) corresponds

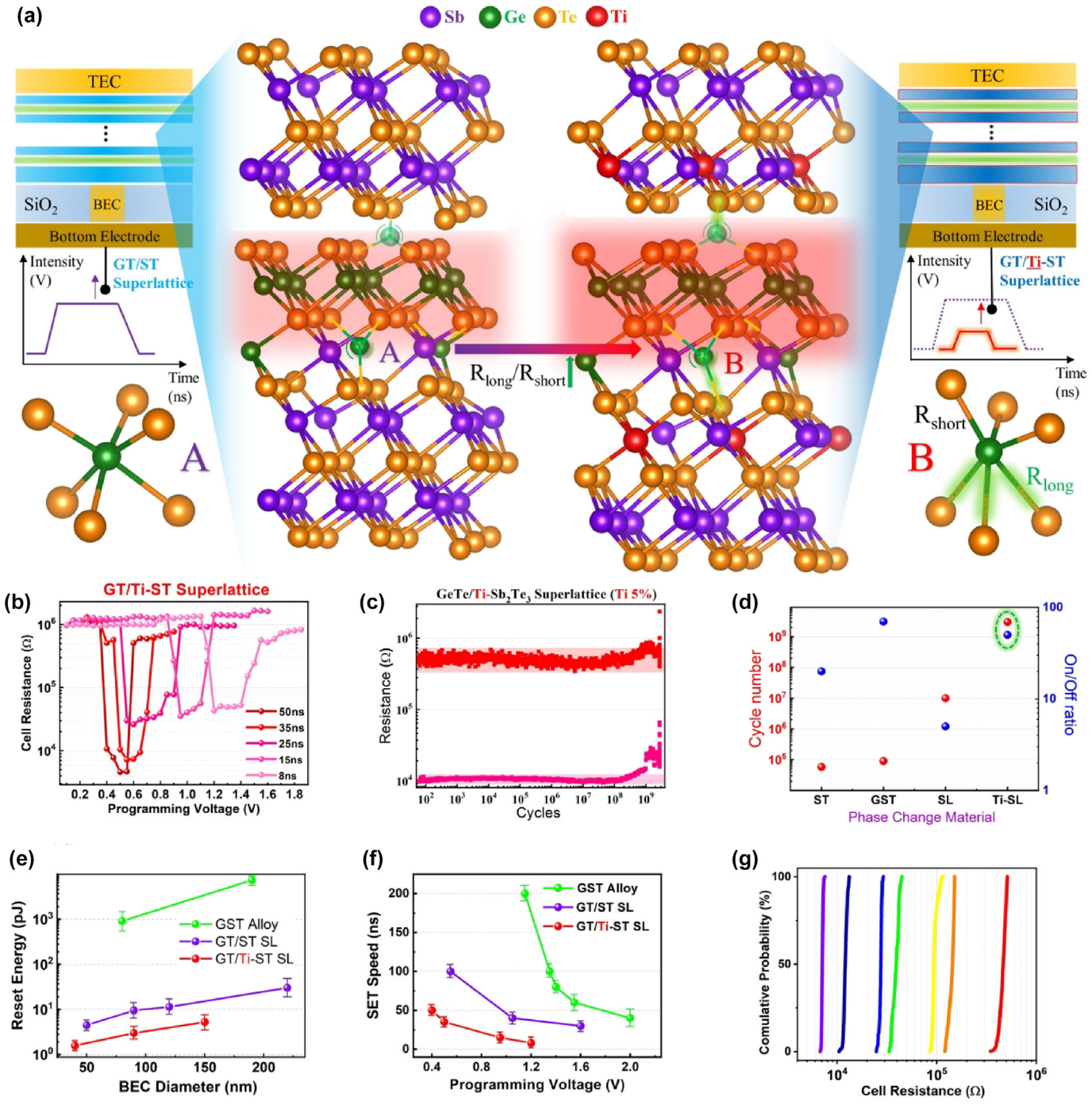

FIG. 1

Scheme and device operation (Scheme of the superlattice structure, device and electrical data obtained from square pulses) a) Schematics of the GT/ST SL and GT/Ti-ST SL and applied electrical pulses for the device operation are presented. The light green block represents the GeTe layer, the sky blue represents the Sb_2Te_3 layer, and the blue represents the Ti-Sb_2Te_3 layer. The following features are expressed in the central part of the scheme: The interfacial space is quite extended along the vertical direction due to Ti-ST block and the heat confinement effect of ST blocks is further strengthened with Ti incorporation, which facilitates efficient phase change process by localizing heat generated by applied electrical pulses into the GT blocks. Moreover, the diagram presents the distortion of Ge-Te bonds is strengthened as the Ge-Te bonds vicinity to Ti atoms are elongated due to short and strong Ti-Te bonds. **b)** Electrical data obtained by increasing the step pulse programming (ISPP) measurements and **c)** cycling endurance of GT/Ti-ST SL (Ti 5%). **d)** Schematic which presents the properties obtained with cycling endurance test based on different PCMs fabricated and evaluated with same electronics. **e)** RESET energy as a function of bottom electrode contact (BEC) diameter. The above values are obtained using product of the power ($P = V^2/R$, where the cell's resistance varies) and the pulse length ($t \sim$ ns) applied during the operation. **f)** SET speed as a function of the applied voltage bias for GST alloy and superlattice device. In obtaining above measured values of e and f. The standard deviations due to the repeated measurements and leading/trail edges of electrical pulses are indicated by hourglass-shaped icons. **g)** Multi-level states are obtained through cyclability test with proper pulse design, and the population for each resistance is calculated and expressed as a cumulative probability.

TABLE 1

Device characteristics with different PCMs.

Type of Phase Change Materials	GST alloy	Ti-ST alloy [32]	GT/ST Superlattice	$TiTe_2/Sb_2Te_3$ (PCH) [27]	GT/Ti-ST Superlattice
RESET Energy (pJ)	600	750	6	200	2
SET Speed (ns)	30	8	30	8	8
Cycling Endurance	10^{5-12} [62]	10^{7}	10^{7-9}	2×10^{9}	3×10^{9}
Multi-Level States (MLC)	16 [63]	2	4 [24]	8	7

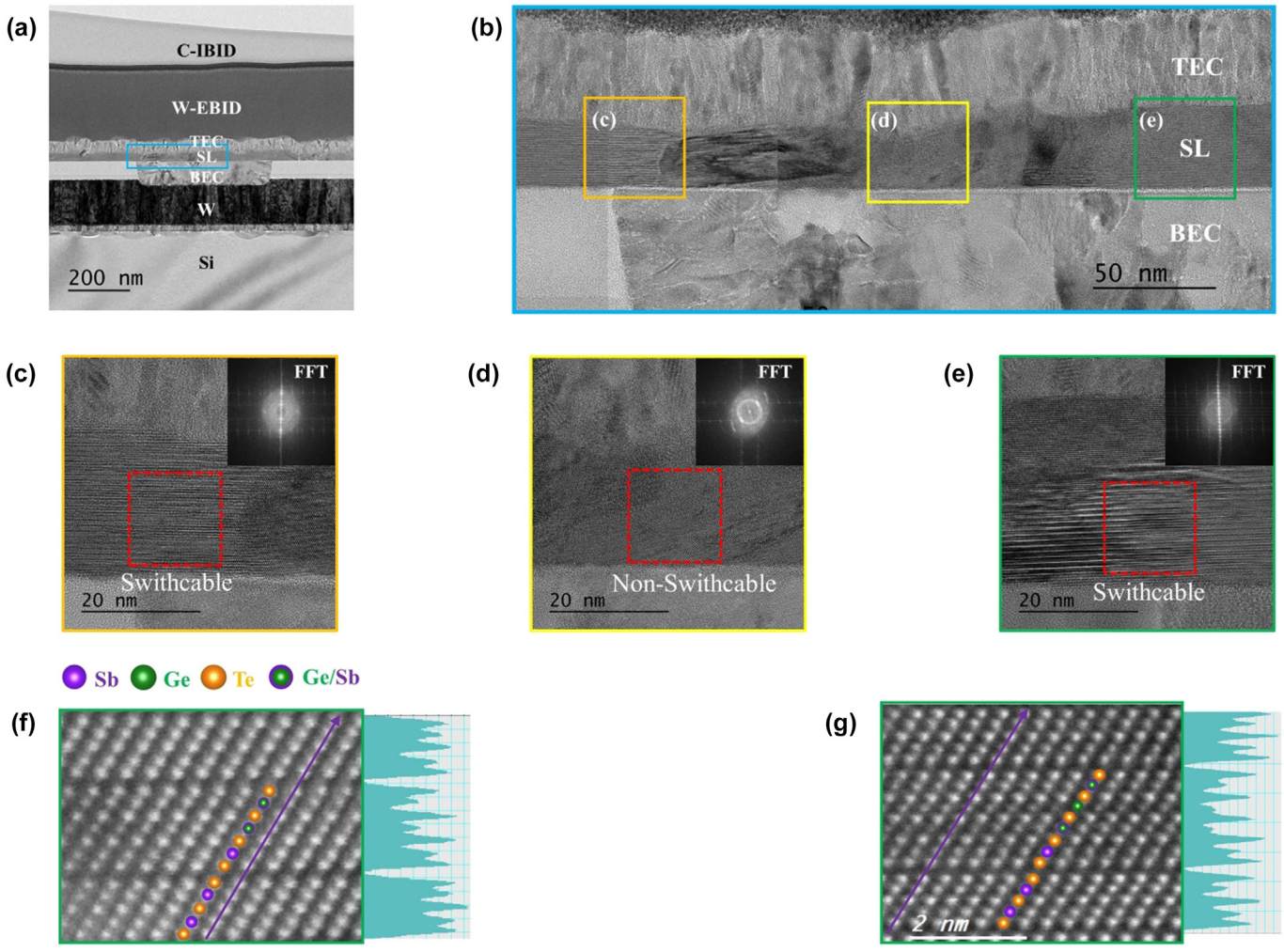

FIG. 2

Transmission Electron Microscope (TEM) results of the superlattice device after the cyclability test. a) TEM image of the superlattice device after cycling operations (~5 × 10^5 times) and **b)** magnified image of a. C-IBID denotes carbon – ion beam induced deposition and W-EBID denotes tungsten – electron beam induced deposition. **c-e)** Magnified images of the area marked with square boxes in b). The degree of crystallization and alignment of each region is presented with fast Fourier transformed (FFT) image. **d)** corresponds to partially amorphous region, which is assumed to be non-switchable. c) and e) correspond to the regions where the layered structures still exist, which are switchable region. **f-g)** is magnified image of e) with intensity profiling where intensity is proportional to Z^2. Valence electrons occupied with p orbital of constituent elements lead to atomic alignment through metavalent bonds. Te is arranged in anion layer and the other elements and vacancy are intermixed in cation layer.

to the LRS since it was measured with low electrical resistance and the atomic alignment is well maintained with the clear interface (vdW gap), while there exist no mis-aligned cation atoms in the vicinity of the vdW layers (Fig. 2f, g).

The hexagonal closed packed (HCP) quintuple layer (QL) structure is also maintained in Ti-ST up to certain amounts of Ti incorporation (Supplementary Fig. 3d, e). To investigate the change in the local structure of Ge atoms at the vdW interface using DFT calculations, unit cells of GT/(Ti)-ST SL were constructed using Ferro structure taking Ge/Sb intermixing [26] into account to reflect the experimental environment. Fig. 3a present unit cell structures with charge density differences in GT/(Ti-)ST,

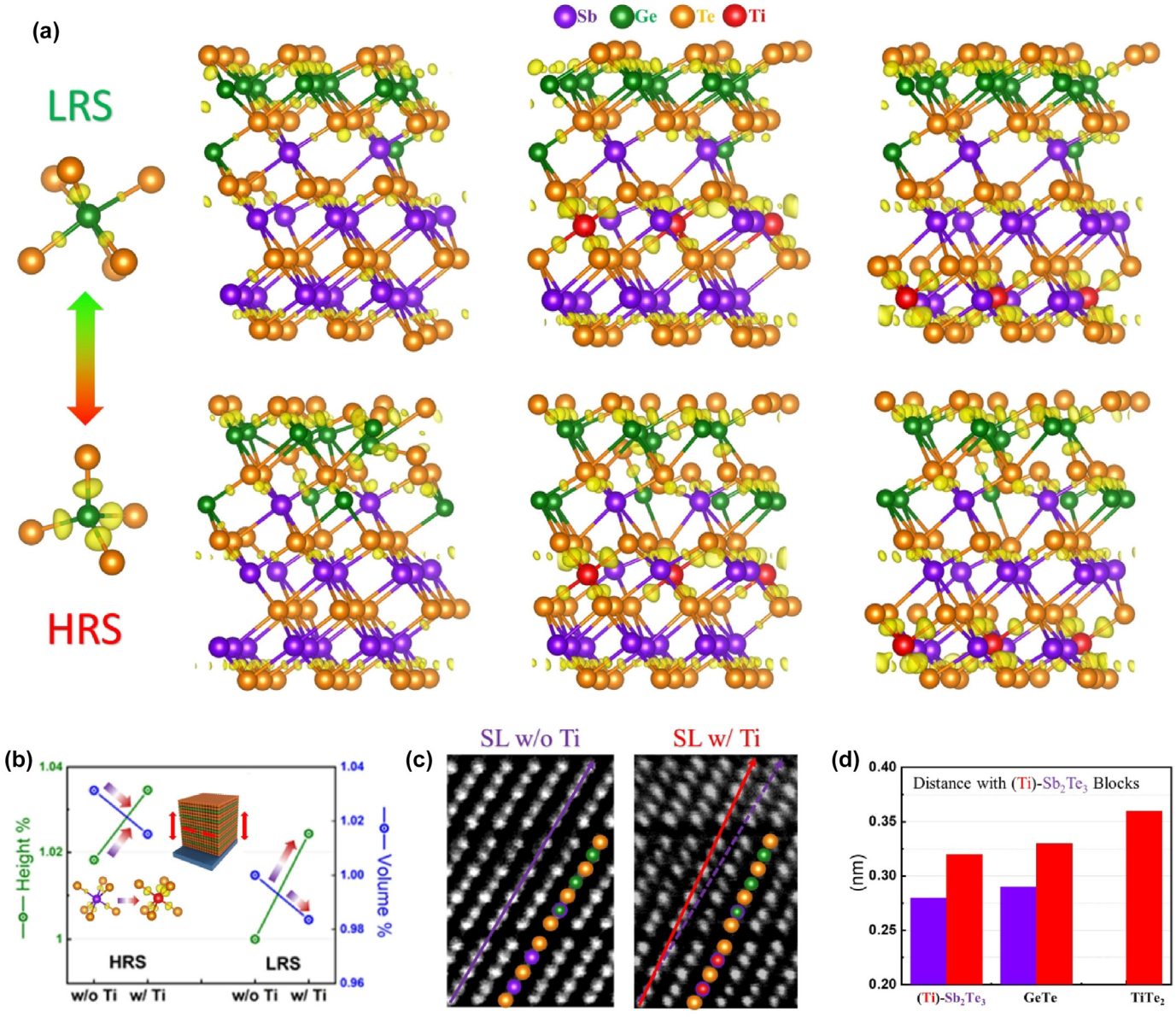

FIG. 3

Unit cell of GT/(Ti-)ST SL and structural changes due to Ti incorporation. DFT modeling of GT/(Ti-)ST SL based on Ferro structure with Ge/Sb intermixing. Strong localization due to Ti incorporation is confirmed with isosurface value being set as 0.008 e/bohr^3. **a)** The upper models are unit cells which correspond to conducting states where all the Ge atoms maintaining octahedral motif, and the lower models correspond to relatively higher resistance states due to the occurrence of some Ge atoms' tetrahedral bonding motif due to site switching between Ge and adjacent vacancies. **b)** The changes in volume and length of the unit cell of LRS/HRS in GT/(Ti-)ST SL. For both reversible phases, Ti leads to reduction of unit cell volume and extension the vdW gap along the c-axis. **c)** HAADF-STEM images of GT/(Ti-)ST SL in LRS. Original atomic alignment is distorted with Ti incorporation. **d)** The distance (vdW gap) between (Ti-)ST block and adjacent blocks through HAADF-STEM measurement in GT/(Ti)-ST SL, purple for distances with ST and red for Ti-ST.

where Ti atoms substitute Sb atoms maintaining the same octahedral motif in ST [25]. Since Ge-Te bond sharing Te with strong Ti-Te bond is relatively weaker than Ge-Te bond near the Sb-Te bond, it is easier for Ge to break the Ge-Te bond near the Ti-Te and convert into the other bonding motif, which is resulted with the electrical switching properties [41]. Phase change process was implemented through the change in the bonding structure of Ge atoms near cation-intermixed zone by site switching between several Ge atoms and adjacent vacancies. Specifically, three relatively long bonds among the six Ge-Te metavalent bonds (2 centor – 1 electron system) [42] combining with octahedral motif are broken and valence electrons occupied in Ge atoms' 4 s orbital additionally participate in new Ge-Te bond with previously participating electrons in 4p orbital forming sp3 hybridized tetrahedral motif. It is confirmed that the bond type of GeTe is changed from metavalent to covalent (2 centor – 2 electron system) bond (Fig. 4d-e) through bond order with DDEC6 method, which present the amount of electrical charge per chemical bond. It is also confirmed that the band gaps between valence band maximum (VBM) and conduction band minimum (CBM)

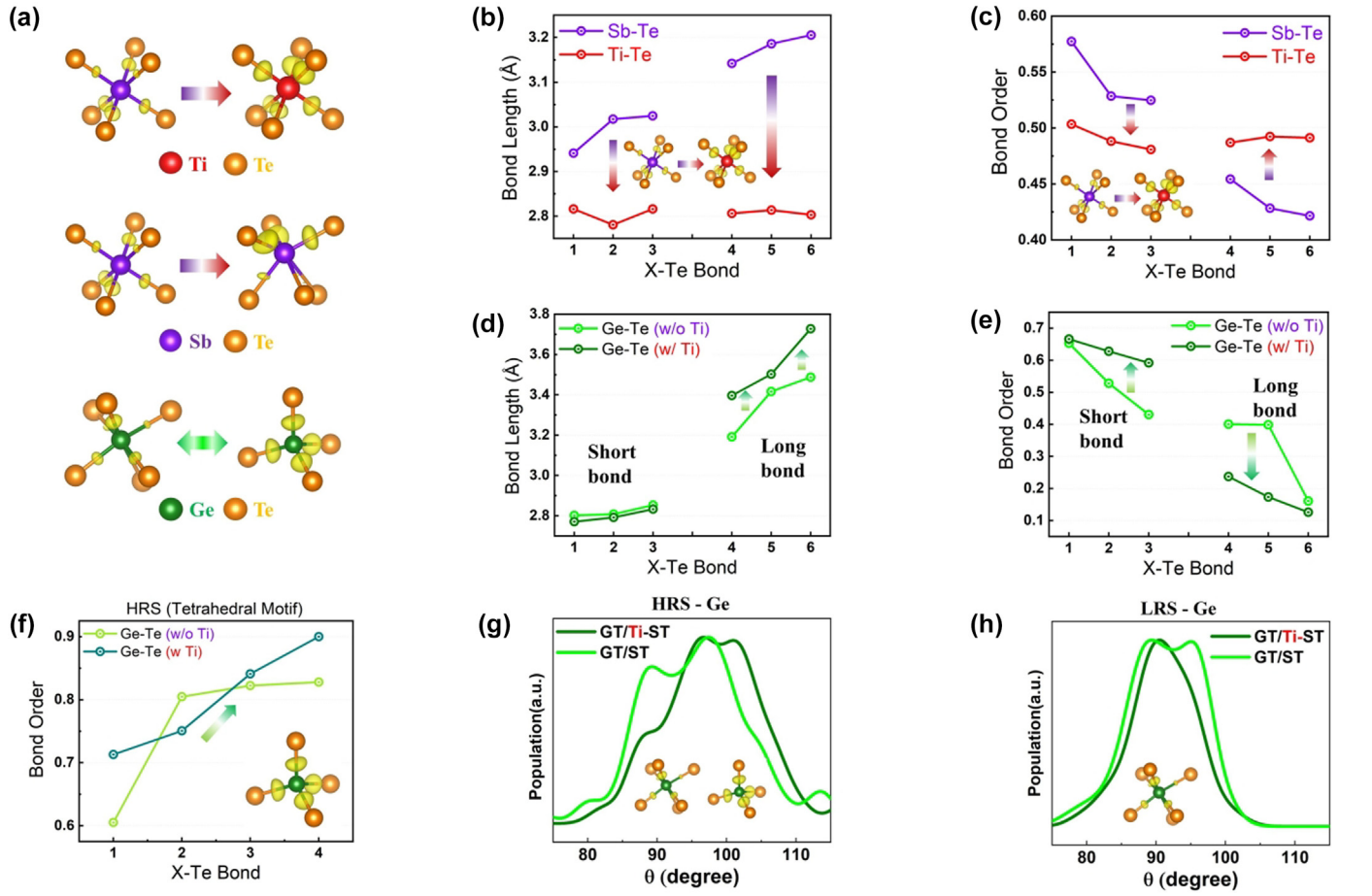

FIG. 4

Bond properties in GT/(Ti)-ST SL. a) Characterization of the chemical bond with the nearest Te atoms, atoms in the center remain Sb, Ti, Ge. Electron density of each atom is 0.005 e/bohr^3. The bond order in these systems corresponds to the value which is dividing the number of valence electrons occupied in the chemical bond between atoms by the number of atoms participating in the bond. **b)** Bond length and **c)** Bond order values for the chemical bonds where Sb and Ti at the center are bounded to Te maintaining octahedral motifs in GT/(Ti)-ST SL. **d)** Bond length and **e)** Bond order values for chemical bonds where Ge at the center is bounded to Te maintaining octahedral motifs in GT/(Ti)-ST SL. **f)** Bond order of Ge at the center are bound to Te with covalent bonding maintain tetrahedral motifs in GT/(Ti)-ST SL. **g-h)** Angle distribution function (ADF) of Ge atoms in GT/(Ti-)ST SL for two reversible phases.

in the band structures corresponded to the unit cells are extended due to site switching between several Ge atoms and adjacent vacancies in the intermixed cation layers (Supplementary Fig. 4e-h). Analyzing the amount of the occupied electrical charge in the bond between Ge atoms and adjacent Te atoms, the change in structural motifs (octahedral or tetrahedral) and bond types (metavalent or covalent) before and after the phase change process can be successfully explained [43,44]. It is interesting that all elements are combined with metavalent [42,45] bonds in LRS of GT/ST SL where valence electrons are occupied with p orbital, maintaining the octahedral bonding motif. It is confirmed that strong p orbital alignment is well established with LRS in the GT/ST SL (Fig. 2f-g) and left side of Fig. 3c. This alignment is due to all constituent elements maintaining octahedral motif and forming metavalent bonds with valence electrons occupied in p orbital [44]. Structural change occurs from octahedral to tetrahedral motif for Ge atoms when phase change proceeds, three relatively weak bonds among the six metavalent Ge-Te bonds in LRS are broken and new identical covalent bonds are formed through sp3 hybridization [46]. On the other hand, unlike Ge atoms, Sb and Ti atoms maintain the same octahedral bonding motif with slight distortion [47]; therefore, a structural change does not occur in (Ti-)ST. Ti maintains octahedral motif through robust Ti-Te bond substituting Sb and HCP QL structure is also well maintained. However, the original p orbital alignment is distorted due to spatial expansion vicinity to the interfaces as well as enhanced structural localization due to robust Ti-Te bond (Fig. 3b-d).

Ti atoms substituting Sb atoms pull nearest Te atoms strongly (Fig. 3), which produce relatively elongated Ge-Te bonds in the intermixed zone. Bond properties were investigated using density derived electrostatic and chemical (DDEC) 6 method (Fig. 4) [43]. Changes in bonding characteristics due to Ti doping are presented in Fig. 4a-c. Ti substituting Sb in the octahedral motif forms six strong and short bonds with Te, which extends the near chemical bond length or vdW gap distance (Fig. 3c-d). The localization in Ti-ST block by Ti-Te bond is strengthened (Fig. 4b-c). Thus, the more Ti atoms are involved in the cation site in the HCP ST block, the stronger the localization within the block, resulting in increased adjacent vdW gap

distance. Volume of unit cell is reduced due to the short and strong Ti-Te bond, while length along the c-axis is rather extended. For V_2VI_3 or Pn_2Ch_3 (Pn = Pnictogen, Ch = Chalcogen) materials, such as Sb_2Te_3 and Bi_2Te_3, constituting HCP QL structure, the vdW gap is significantly reduced compared with theoretically expected value due to metavalent bonding of the electrons at the interface [48]. However, shrinkage of interfacial space is relieved as interfacial metavalent bonding is decreased to some extent due to incorporated Ti in GT/Ti-ST SL. Since the phase change in iPCM occurs with limited atomic movement of Ge atoms vicinity of the interface [49], expanded interfacial space facilitate the vertical movement of Ge atom, which occurs with phase change process. This result strongly suggests that the performance of GT/ST SL can be successfully improved by controlling the interfacial characteristics by modifying specific layers in iPCM structure: i.e., iPCM can be improved with inducing the interfacial confinement effects. The increased portion of bonding motif change in GT/(Ti)-ST SL with site switching between the same number of Ge atoms and adjacent vacancies is due to the extended interfacial space (Fig. 4g, h). The length of chemical bonds between Ge atom located in Ge/Sb intermixed zone and Te which is pulled toward Ti is increased and the amount of electrical charge involved in the bond is decreased (Fig. 4d, e). Ge-Te bonds near Ti atoms are easier to break by the strengthened Peierls distortion (R_{long}/R_{short}) [50] due to elongated Ge-Te bonds close to Ti atoms. Therefore, Ge atoms located in Ge/Sb intermixed zone are much easier for switching to the other structural motif compared with environment without Ti. Since Ge atoms bonded with adjacent Te atoms have relatively increased vacant space along the c-axis, they can be easily flipped to tetrahedral motifs. It is well understood that Ge in the center forms covalent bonds with four Te atoms with almost same bond length. The closer the bond order value is to 1, the greater the amount of the occupied electrons in the bond, which denotes the strong covalent bonding motif [51]. This tendency is more evident in GT/Ti-ST compared with GT/ST (Fig. 4f-h). Analyzing angle distribution function (ADF), it is confirmed that bond angle of Ge atoms was much more distributed around 100° in GT/Ti-ST SL than in GT/ST SL, corresponding to phase change with the local structural changes of Ge atoms. Ti and Sb always maintain octahedral motifs, bond angle near 90° [52,53], regardless of the structural change, while Ge atoms partially change to tetrahedral motif (covalent bonding with Te atoms) in HRS (Supplementary Fig. 5). Sb always maintains an octahedral motif in GT/(Ti-)ST SL, which forms partially defective octahedral motifs regardless of phase change process, including elongated Sb-Te bonds due to Ti [52]. Ti is maintaining strong octahedral motif with short and strong Ti-Te bond.

The structural/bonding properties in GT/Ti-ST superlattice

Significant improvements in GT/Ti-ST superlattice films with Ti incorporation are also elucidated through several structural analyses. Using time-domain thermo-reflectance (TDTR) measurement, the decrease in thermal conductivity of iPCM was confirmed. It is very interesting that the reduction in thermal conductivity of 5%-doped GT/Ti-ST is larger than the 10% doped Ti-ST SL (Fig. 5a-b). This is caused by generation of $TiTe_2$ from Ti-ST block with excess amount of Ti (Supplementary Fig. 3f-i). Tri-layered $TiTe_2$ blocks have large lattice mismatch about 11% with GT and ST, which deteriorate the formation of uniform interfaces in superlattice structure [54]. For GST based PCM, thermal conductivity along the cross-plane is lowered in superlattice structure than in alloy due to increased anisotropy and presence of the vdW interface [55]. Ti-ST has lower thermal conductivity than ST system [32]. Therefore, it has more efficient intrinsic thermal barriers inside the superlattice structure when Ti is incorporated with certain amounts in ST blocks. Since PCM operates with Joule-heating process, lowered thermal conductivity of GT/Ti-ST SL helps confine the generated heat with applied electrical pulses inside the active region, which enable ultra-low energy switching for GT/Ti-ST SL [56,57]. The scheme and TEM image of superlattice device presented in Fig. 2 and the red box (Fig. 1a) illustrate the strengthened thermal confinement effect of ST blocks due to Ti incorporation with lowered thermal conductivity.

Another important role of Ti is in synthesizing an ideal iPCM by inducing the coherent growth of HCP QL ST and GT blocks by changing the process of forming HCP QL ST blocks from growth-dominant to nucleation-dominant method, which prevent deterioration of the roughness due to abrupt change of grain size during the synthesizing process [32]. By incorporating Ti atoms in iPCM, it is possible to synthesize an iPCM with uniform vdW layers over large areas. From X-ray diffraction (XRD), X-ray reflectance (XRR), and atomic force microscope (AFM) results, it is confirmed that morphology of iPCM is significantly improved by an appropriate amount of Ti and that good crystallinity is maintained (Fig. 5c-e).

In addition, the chemical states of composed elements are studied using XPS, with an in-situ transfer system to prevent oxidation, to obtain accurate bonding state of the constituent elements, measured chemical states showed that there were no phase segregations despite Ti is incorporated and it is observed that all elements except for Te atom itself are combined with Te (Fig. 5f-i). The binding energy shift for constituents almost did not occur before and after doping. That is, the chemical circumstance of Ti bonded with Te is hardly modulated, resulting in the maintenance of the octahedral motif [52]. It is also confirmed with crystal orbital Hamiltonian population (COHP) calculations that antibonding states which exist beneath the fermi level energy in HCP Sb-Te bond do not exist in the HCP Ti-Te bond, which leads to the improved structural stability in the confinement barrier due to robust Ti-Te bond (Supplementary Fig. 6). In addition to the structural stability, it is confirmed that the thermal stability of GT/Ti-ST SL is higher than that of GT/ST SL by measuring the maintenance of the c-axis superlattice structure with XRD under subsequent thermal annealing (Supplementary Fig. 9). From above, GT/Ti-ST SL can avoid device failure due to formation of segregated phases with additional element. The atom that plays a key role in the phase change process is Ge atom (Supplementary Fig. 4a-b). Therefore, the phase change mechanism in GT/Ti-ST SL is up to the behavior of Ge atoms as the same manner in GT/ST SL. In addition, only valence electrons occupied in p orbital participate in chemical bonding maintaining the p orbital alignment in LRS where the octahedral motif is maintained for all elements. It is also confirmed that the

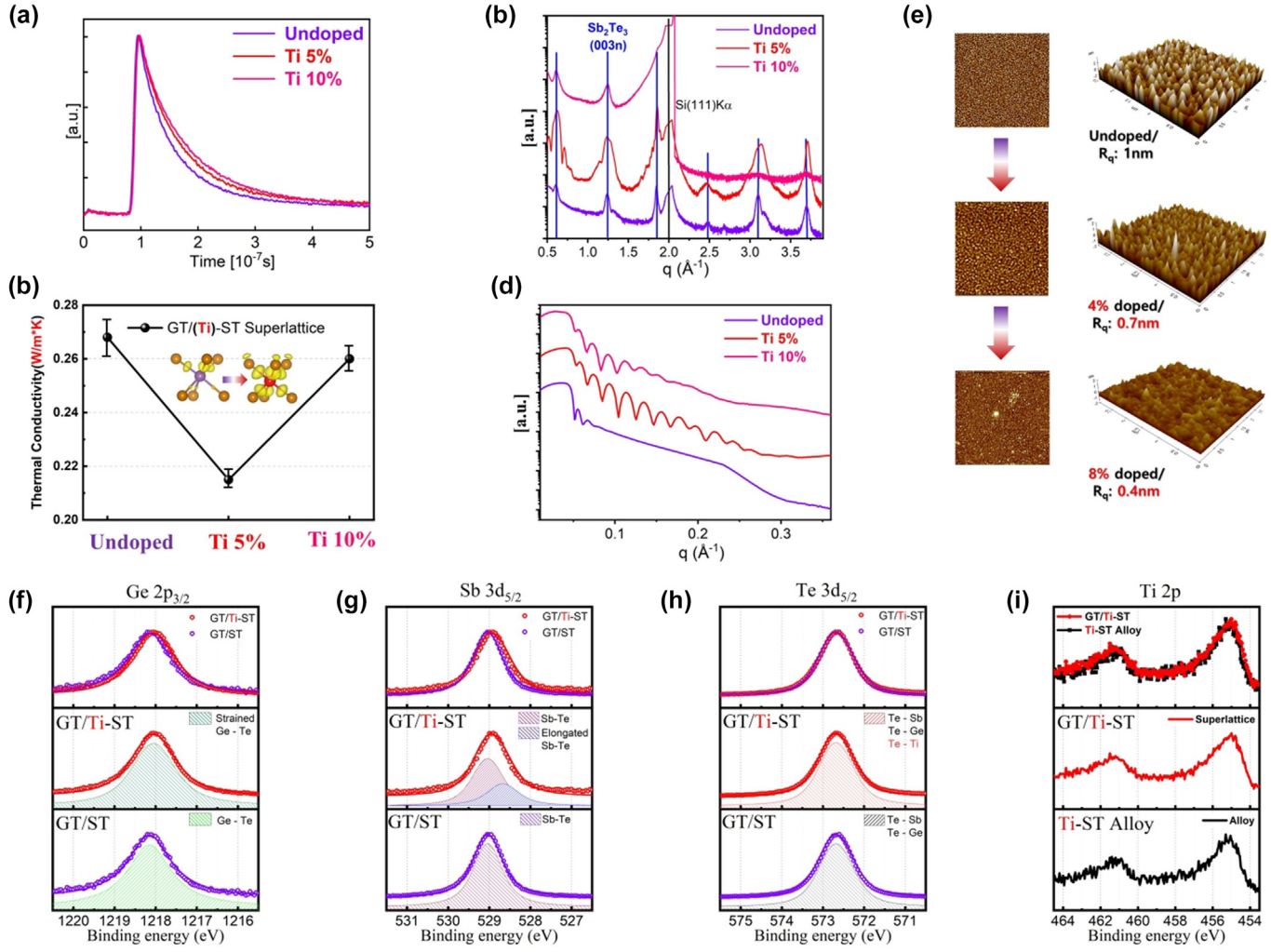

FIG. 5

Structural analysis in GT/(Ti-)ST SL. a) Raw data of the time-domain thermo-reflectance (TDTR) data and **b)** thermal conductivity of GT/(Ti)-ST SL. Above standard deviation occurs during the fitting operation, which is to minimize the root-mean-square error through the iterative optimization process. **c)** X-ray diffraction (XRD) and **d)** X-ray reflection (XRR) measurement of GT/(Ti)-ST SL on Si (1 1 1) substrate through θ-2θ method. **e)** Atomic force microscope (AFM) data of GT/(Ti)-ST SL on Si (1 1 1) substrate. X-ray photoelectron spectroscopy (XPS) data of each element, which corresponds to **f)** Ge, **g)** Sb, **h)** Te, **i)** Ti of GT/(Ti)-ST SL and Ti-ST alloy. Sb 3d peak is broadened asymmetrically because Sb $3d_{5/2}$ peak maintaining octahedral motif is deconvoluted to two peaks corresponded to elongated and original bond due to short and strong Ti-Te bonds, which is consistent with the results of the micro-structural change (Fig. 4d-e).

distortion of the p orbital alignment and chemical states of Ge element and overall band structures change as a few Ge atoms' bonding motif changes from the octahedral to tetrahedral motif with adjacent Te atoms in the vicinity of the interface (Supplementary Fig. 5) through TEM (Supplementary Fig. 7) and XPS measurements and DFT calculations (Supplementary Fig. 4) when the sufficient electrical pulses or additional thermal heat are applied to the superlattice. Reversible phases of GT/(Ti)-ST SL show different crystal structures and physical properties depending on Ge atoms' bonding motif (octahedral or tetrahedral), but the phase change process of the materials still proceed with Joule heating process. Considering the reported research [9], it is probable that phase change process between the two reversible crystal structures proceeded through a transient molten phase in the interfacial region, and thermally insulating robust Ti-ST layers can perform this confinement template role better than ST layer.

Moreover, analyzing composition ratio using XPS measurement showed that the GT/(Ti-)ST SL structure has Ge-deficient GT layers (Tabls S1). In detail, the result indicates that intrinsic vacancies from the cation site in GT layer help Ge to move efficiently during phase change process, which is consistent with already reported research that Ge-deficient GT layers contribute to superior phase change properties in iPCM [6,58]. In this research, the synthesis of GT/(Ti)-ST SL were carried out under lower temperature (lower than 200′C) than the previously reported synthesis temperature of GT/ST SL. Therefore, it is thought that Te-rich superlattice was obtained since the desorption rate of Te during deposition process was lower than that of the previously reported GT/ST SL (230–250′C) [59].

Conclusions

In summary, an ultra-efficient and structurally coherent advanced iPCM was developed in this study, which led to the following figure of merit: high cycling endurance ($\sim 3 \times 10^9$), ultra-low RESET energy ($\sim$2 pJ), and high speed ($\sim$8 ns). After sufficient electrical pulsing, it is observed that internal structure of superlattice device was well maintained, i.e., Te terminated layers were preserved. It was confirmed through intensity profiling that 7 and 9 layered Ge/Sb intermixed GT blocks including intrinsic vacancies are strongly aligned between (Ti-)ST quintuple layers. Interestingly, it is also confirmed that strong p orbital alignment in GT/ST SL is slightly distorted with Ti due to the strong localization. Based on Ferro(-like) structure including Ge/Sb/vacancy intermixing, bonding properties of two reversible phases in GT/(Ti)-ST SL are analyzed with DFT calculations and XPS. Ge-Te bonds vicinity to Ti-Te bonds are elongated, which facilitate Ge atoms to break the original bond with Te by strengthened Peierls distortion (R_{long}/R_{short}). Although volume size of unit cell is reduced as intra-structural localization of ST block is strengthened by incorporating Ti atoms in ST blocks, interfacial space is expanded. The phase change process is strengthened with the stable structure formed by strong intra-structural localization and reduced antibonding states of Ti-Sb_2Te_3 blocks and switching energy consumption is reduced with enhanced thermal barrier effects by lowered thermal conductivity with Ti. Considering recent research have been still reporting that the phase change behavior of GT/ST SL proceeds through the melt-quenching process as the same way of conventional GST alloy, strengthening the heat confinement effect of the thermal template (ST layer) with incorporated Ti elements contribute to the superlattice system's reduced energy consumption while maintaining existed chemical bonds of the constituent elements. GT/Ti-ST SL improved the overall phase change characteristics of the GT/ST SL system by appropriately widening the vdW gap without dramatically changing the existed bonding motif while it reinforces the thermal and structural stability by reducing perpendicular thermal conductivity and antibonding states near E_F. In addition to GT/Ti-ST SL's strong figure of merits for cycling endurance and low-energy transition by effectively reducing entropic loss during phase change process, elaborated resistance changes with repetitive electrical pulsing and suppressed resistance drift become possible due to the improved structural coherence and stability. By selectively modifying properties of confinement layer through doping with other transition metals which enable to strengthen structural coherence and confinement effect of Sb_2Te_3 block of iPCM, other advanced iPCMs can be developed to be energy efficient and have high thermal/structural stability and operating limit. Unlike the original modifying methodologies which uniformly control the entire region of the alloy based PCM, superlattice based PCM could be engineered to improve the phase change characteristics of the entire system and ensure efficient phase-change operation characteristics by controlling the confinement layer selectively. Advanced iPCM is expected to pave the way for developing advanced memory devices by suppressing wasted heat generated during the phase change process and effectively forming structurally coherent interfaces, which leads to the stable multi-level states. Advanced iPCM has an enormous potential to be one of the strongest candidates for non-volatile memories in highly integrated memory systems such as cross bar array architecture, which is suitable to perform deep learning operations with matrix–vector-multiplication in neuromorphic computing [35,60,61].

Methods

Sample Preparation. The thin film preparation process for structural analysis is as follows: iPCM is synthesized with MBE. In the case of molecular beam epitaxy, the substrate is fixed at the center of the upper range under high vacuum (base pressure $\sim$high 10^{-9} Torr) and the constituent elements of the material to be deposited are evaporated in gaseous form onto the substrate through thermal evaporation. When synthesizing the film on the silicon substrate, which is oriented in the (1 1 1) direction, the substrate (silicon wafer) is soaked in acetone and isopropanol successively for a few minutes to desorb organic matter, ultrasonicated, and soaked in a buffered oxide etchant to remove the native oxide (SiO_2) of the substrate, and finally, rinsed with deionized (DI) water. Then, the Si wafer is transferred to the MBE chamber and annealed at a high temperature (about 600 °C) to remove the remaining impurities, cooled to room temperature, and then Ti-ST is deposited at room temperature with a thickness of 3 nm. Heat treatment at 190 °C (for the 5% doping; the higher the doping percentage, the higher the required heat treatment temperature) for 30 min follows, and then 4–5 nm of Ti-ST is stacked while maintaining the above temperature. A robust seed layer is formed through the above two-step process. After lowering the temperature slowly to about 20 °C, the temperature of the effusion cell containing each element is adjusted to evaporate each source with the intended ratio (1.0 Å/min for Ge, 1.5 Å/min for Sb, 3 Å/min for Te, and about 0.4 Å/min for Ti). Each source (Ge, Sb, Te) is heated in an isolated Knudsen cell containing a cylindrical crucible, and then a beam of each component directed toward the substrate is ejected from the cell and adsorbed on the surface. Ti is evaporated with an e-beam evaporator where a hot electron beam is generated from the filament and accelerated by an electric/magnetic field; it hits the source rod to vaporize Ti from the source and then transfer it to the substrate. Each material has a different desorption rate depending on the selectivity of the substrate and the pre-deposited material. Considering this, the deposition rate on the substrate surface is precisely controlled through the Proportional-Integral-Differen tial (PID) controller to enable the precise control that responds to every moment for the growth of a very high-quality thin film. After synthesizing the seed layer and lowering the temperature to about 20 °C, approximately 1 nm of the GT layer and approximately 2–3 nm of Ti-ST is deposited alternately. The above process is repeated until the top layer (Ti-ST) is deposited.

X-Ray Diffraction/Reflection (XRD/XRR). The XRD measurement is performed using a high-resolution X-ray diffractometer with a 9 kW Cu Kα (wavelength $\sim$1.5406 Å) radiation source. The measurement was conducted with the Po-hang accelerator 5D beam line.

Raman Spectroscopy. Raman spectra were obtained through micro-Raman spectroscopy (Horiba Lab Ram ARAMIS) using a 532 nm wavelength Nd: YAG laser with a 100x objective

and 2400 grooves/mm grating. The spectra were calibrated at a silicon peak of 520 cm^{-1}.

X-ray photoelectron spectroscopy (XPS). In-situ XPS spectra of the core levels were measured using the PHI 5000 Versa Probe made by ULVAC-PHI, where the base pressure was about 4×1^{-10} Torr. The XPS spectra were obtained using monochromatic Kα radiation with an analyzer pass energy of 23.5 eV, providing an overall experimental resolution of 200 meV. The background of each spectrum was subtracted by the Shirley method. For the depth profile, a 500 kV $Ne^{\pm}$ ion beam was used, a modest condition to prevent transformation of the samples.

Keithley (I-V test). To probe the operation of the test cells, an Agilent 33600A pulse generator and a Keithley 2636B sourcemeter were used for applying electrical pulses and measuring the resistance during the switching process, respectively. To switch the cells between several reversible phases, electrical pulses which were 8–200 ns in width and 0.1–3 V in height were applied, and each state's resistance was measured at 0.1 V.

Transmission Electron Microscope (TEM). TEM specimens for cross-sectional observation of the super-lattice devices were prepared using a focused ion beam (FIB, NX2000; Hitachi Inc., Japan) instrument. To maintain the initial state of the specimen, tungsten and carbon were used as protective layers. During the FIB process, the TEM specimen was etched with $Ga^{\pm}$ ions at 30 kV, 10 kV, and 5 kV, successively. The TEM images were taken at an accelerating voltage of 200 kV using a JEM-ARM200F (JEOL Ltd.) and One View camera (Gatan Inc.). The STEM images were acquired at an accelerating voltage of 200 kV using an aberration-corrected STEM (JEM-ARM200F, JEOL Ltd.). STEM images were collected using a convergence semi-angle of 21 mrad and a high-angle annular dark field (HAADF) detector with a collection semi-angle of 68–280 mrad. Additional TEM data are added in supplementary figure sets during the revision courses. The microstructures characterized by transmission electron microscopy (TEM, JEM-ARM200F "NEO ARM," JEOL) and energy-dispersive X-ray spectrometry (EDS, JED-2300 T(Dual), JEOL) at Yonsei Center for Research Facilities, Yonsei University. TEM and scanning TEM (STEM) observations were conducted at an accelerating voltage of 200 kV.

Density Functional Theory (DFT) Calculation. The electronic structures of the GT/(Ti-)ST SL were calculated using DFT with the Vienna Ab initio Simulation Package (VASP) [64]. All calculations were implemented at the generalized gradient approximation level, using the Perdew-Burke-Ernzerhof (PBE) [65] functional. The Grimme's D3 [66] dispersion correction term was added to capture long-range interactions during structure optimization. The Brillouin zone was sampled 3×3×1 for relaxation and 7×7×5 for single-point calculations, the kinetic energy cutoff for the plane wave was set to 500 eV , and the convergence criterion for the self-consistent loop was 1E-6 eV for optimization (single-point calculation) until the difference in force between the steps was less than 0.01 eV/Å. The superlattices were relaxed with 2 × 2 × 2 Brillouin zone sampling and gamma point sampling, respectively. By fabricating several 3 × 3 × 1 supercells of ST, representative structures were created in which Sb and vacancies were mixed in a ratio of 2:1 in all layers except for the Te layers. The exact location of the vacancy was determined by the CD and monitored during the process of site switching and optimization. Subsequently, the CD near the vacancy site was numerically integrated. The superlattices were constructed in the same manner. The vacancies, Sb, and Ge were mixed at the interface between GeTe and ST. The bond order was calculated using the density derived electrostatic and chemical (DDEC6) approach [43]. The band structure calculations were carried out in the reciprocal space along the symmetry points (K, Γ, M). The structures were visualized through VESTA program.

Time-Domain Thermo-Reflectance (TDTR). To measure the thermal metrology based on thermo-reflectance, the N8- 200 made by TMX Scientific Transometer™ was used. A pulsed heating laser of 4.7–5.8 μJ was illuminated to change the temperature of the surface and heat reflection energy of the sample with the film stack. At the same time, a probing laser (18.5–23.3 mW) was used to record the change in light reflectivity (i.e., thermal decay) as a function of time. Two unknown independent parameters can be extracted after fitting by combining the experimental data with known material parameters. These unknown parameters can be calculated using the coefficient of thermal reflectance, representing the relationship between temperature and reflectivity changes. During the fitting process, optimal calculations were performed through an iterative optimization process that minimized the root-mean-square error between the experimental and numerical decay curves. Eventually, the inverse numerical solution can acquire the film stack's thermal conductivity and boundary resistance.

CRediT authorship contribution statement

Hyeonwook Lim: Conceptualization, Data curation, Formal analysis, Investigation, Methodology, Project administration, Writing – original draft, Writing – review & editing. **Young sam Kim:** Data curation, Formal analysis, Methodology, Resources. **Kyu-jin Jo:** Data curation, Methodology, Resources. **Seok-Choi:** Data curation, Methodology, Resources. **Byung-Joon Choi:** Supervision, Formal analysis, Resources, Writing – review & editing. **Cheol-Woong Yang:** Supervision, Formal analysis, Resources, Writing – review & editing. **Eun Ji Sim:** Supervision, Formal analysis, Resources, Writing – review & editing. **Mann-Ho Cho:** Supervision, Formal analysis, Project administration, Resources, Writing – review & editing.

Data availability

Data will be made available on request.

Declaration of Competing Interest

The authors declare that they have no known competing financial interests or personal relationships that could have appeared to influence the work reported in this paper.

Acknowledgements

This research was supported by grants from the Government of Korea (MSIP) (No. 2021M3H4A1A03052566) and the Korea Semiconductor Research Consortium (KSRC) through a project developing source technologies for future semiconductor devices and NRF-2020R1A2C2007468 for DFT Calculations and sup-

ported by the National Research Foundation of Korea (NRF) grant funded by the Government of Korea (MSIP) (No. 2020M3F3A2A01082324) and supported by the National Research Foundation of Korea (NRF) grant funded by the Korea government (MSIT) (grant No. 2022M3I7A2079098). We would like to thank Editage (www.editage.co.kr) for English language editing.

Appendix A. Supplementary data

Supplementary data to this article can be found online at https://doi.org/10.1016/j.mattod.2023.07.025.

References

[1] A.V. Kolobov et al., Nat. Mater. 3 (2004) 703–708.
[2] G.W. Burr et al., J. Res. Dev. 52 (2008) 449–464.
[3] M. Salinga et al., Nat. Mater. 17 (2018) 681–685.
[4] Y. Xie et al., Adv. Mater. 30 (2018) 1705587.
[5] S. Ghazi Sarwat et al., Adv. Funct. Mater. 31 (2021) 2106547.
[6] J. Tominaga, Phys. Status Solidi – Rapid Res. Lett. 13 (2019) 1800539.
[7] R.E. Simpson et al., Nat. Nanotechnol. 6 (2011) 501–505.
[8] K.V. Mitrofanov et al., Phys. Status Solidi – Rapid Res. Lett. 13 (2019) 1–6.
[9] M. Behrens et al., Nanoscale 10 (2018) 22946–22953.
[10] C. Woo Lee et al., Surf. Sci. 602 (2022) 154274.
[11] M. Boniardi et al., Phys. Status Solidi – Rapid Res. Lett. 13 (2019).
[12] D. Térébénec et al., Phys. Status Solidi – Rapid Res. Lett. 15 (2021) 1–9.
[13] K.L. Okabe et al., J. Appl. Phys. 125 (2019).
[14] A. Lotnyk et al., Appl. Surf. Sci. 536 (2021) 147959.
[15] A. Lotnyk et al., Nanoscale 11 (2019) 10838–10845.
[16] J. Feng et al., Mater. Interfaces 12 (2020) 33397–33407.
[17] B.J. Kooi, J. Momand, Phys. Status Solidi – Rapid Res. Lett. 13 (2019) 1800562.
[18] T. Ohyanagi et al., Appl. Phys. Lett. 104 (2014) 252106.
[19] J. Tominaga et al., Adv. Mater. Interfaces 1 (2014) 1300027.
[20] K.V. Mitrofanov et al., Phys. Status Solidi – Rapid Res. Lett. 13 (2019) 1900105.
[21] X. Yu, J. Robertson, Sci. Rep. 5 (2015) 1–8.
[22] J. Kalikka et al., Nat. Commun. 7 (2016).
[23] X. Zhou et al., Adv. Mater. 28 (2016) 3007–3016.
[24] A.I. Khan et al., Science 373 (2021) 1243–1247.
[25] M. Zhu et al., Nat. Commun. 5 (2014) 4086.
[26] J. Tominaga, S. Sumi, H. Awano, Appl. Phys Express 13 (2020) 075503.
[27] K. Ding et al., Science 366 (2019) 210–215.
[28] C. Kaspar et al., Nature 594 (2021) 345–355.
[29] W. Zhang et al., Nat. Rev. Mater. 4 (2019) 150–168.
[30] F. Rao et al., Science 358 (2017) 1423–1427.
[31] M. Xu et al., Adv. Funct. Mater. 2003419 (2020) 1–21.
[32] M. Xia et al., Mater. Interfaces 7 (2015) 7627–7634.
[33] A. Sebastian et al., Nat. Nanotechnol. 15 (2020) 529–544.
[34] Q. Xia, J.J. Yang, Nat. Mater. 18 (2019) 309–323.
[35] M. Xu et al., Adv. Funct. Mater. 30 (2020) 2003419.
[36] B. Liu et al., Sci. Bull. 66 (2021) 2217–2224.
[37] J. Momand et al., J. Mater. Res. 31 (2016) 3115–3124.
[38] J. Momand et al., Nanoscale 7 (2015) 19136–19143.
[39] X. Yu, J. Robertson, Sci. Rep. 6 (2016) 37325.
[40] D. Kim et al., ACS Nano 16 (2022) 20758–20769.
[41] C. Ribaldone, D. Dragoni, M. Bernasconi, Nanoscale Adv. 2 (2020) 5209–5218.
[42] M. Wuttig et al., Adv. Mater. 30 (2018) 1803777.
[43] T.A. Manz, RSC Adv. 7 (2017) 45552–45581.
[44] D. Kim et al. (2022).
[45] M. Zhu et al., Adv. Mater. 30 (2018).
[46] A.V. Kolobov, P. Fons, J. Tominaga, Phys. Rev. B 87 (2013) 155204.
[47] Z. Song et al., Nano Res. 15 (2022) 765–772.
[48] Y. Cheng et al., Adv. Mater. 31 (2019) 1904316.
[49] H. Nakamura et al., Nanoscale 9 (2017) 9386–9395.
[50] J. Raty et al., Adv. Mater. 31 (2019) 1806280.
[51] B.J. Kooi, M. Wuttig, Adv. Mater. 32 (2020).
[52] F. Rao et al., Nat. Commun. 6 (2015) 10040.
[53] Z. Song et al., Sci. China Inf. Sci. 61 (2018) 081302.
[54] J. Shen et al., Mater. Interfaces 11 (2019) 5336–5343.
[55] A.I. Khan et al., IEEE Electron Device Lett. 43 (2022) 204–207.
[56] K.L. Okabe et al., J. Appl. Phys. 125 (2019) 184501.
[57] B. Fu, G. Tang, Y. Li, PCCP 19 (2017) 28517–28526.
[58] N. Takaura et al., in: 2014 IEEE Int. Electron Devices Meet., IEEE, 2014, pp. 29.2.1–29.2.4.
[59] Y. Saito et al., J. Phys. D Appl. Phys. 53 (2020).
[60] W. Yang et al., J. Appl. Phys. 129 (2021) 050903.
[61] W. Zhang, E. Ma, Mater. Today 41 (2020) 156–176.
[62] W. Kim et al. (2016) 83–86.
[63] T. Nirschl et al., in: Tech. Dig. - Int. Electron Devices Meet, IEDM, 2007, pp. 461–464.
[64] G. Kresse, J. Furthmüller, Phys. Rev. B 54 (1996) 11169–11186.
[65] J.P. Perdew, K. Burke, M. Ernzerhof, Phys. Rev. Lett. 77 (1996) 3865–3868.
[66] S. Grimme et al., J. Chem. Phys. 132 (2010) 154104.